LAWRENCE
LIVERMORE
NATIONAL
LABORATORY

LLNL-TR-406937

Total Energy Monitor

S. Friedrich

September 11, 2008

Disclaimer

This work performed under the auspices of the U.S. Department of Energy by Lawrence Livermore National Laboratory under Contract DE-AC52-07NA27344.

LCLS Engineering Specifications Document # 1.5-106	X-Ray Transport and Diagnostics	Revision 0

Total Energy Monitor

Stephan Friedrich Author	Signature	Date
Richard Bionta XTOD Manager	Signature	Date
Peter Stefan XTOD Physics Liaison	Signature	Date
John Arthur Photon Systems Manager	Signature	Date
Darren Marsh Quality Assurance Manager	Signature	Date

Summary:

This document summarizes the physics behind the operation of the Total Energy Monitor at LCLS and derives associated engineering specifications.

Change History Log

Rev Number	Revision Date	Sections Affected	Description of Change
000	2008/7/31	All	Initial Version

Disclaimer

Auspices Statements

This work was performed under the auspices of the U.S. Department of Energy by University of California, Lawrence Livermore National Laboratory under Contract W-7405-Eng-48 and also supported in part by the DOE Contract DE-AC02-76SF00515. This work was performed in support of the LCLS project at SLAC.

Executive Summary

The total energy monitor (TE) is a thermal sensor that determines the total energy of each FEL pulse based on the temperature rise induced in a silicon wafer upon absorption of the FEL. The TE provides a destructive measurement of the FEL pulse energy in real-time on a pulse-by-pulse basis. As a thermal detector, the TE is expected to suffer least from ultra-fast non-linear effects and to be easy to calibrate. It will therefore primarily be used to cross-calibrate other detectors such as the Gas Detector or the Direct Imager during LCLS commissioning. This document describes the design of the TE and summarizes the considerations and calculations that have led to it.

I. System Requirements

The Total Energy Monitor (TE) is a thermal sensor designed to determine the total energy of each FEL pulse in real-time on a pulse-by-pulse basis. It is based on measuring the temperature rise induced in a known material upon absorption of the FEL. The LCLS Physics Requirements Document for the TE [1] lists the fundamental requirements for the system. They are briefly summarized here.

1. Radiation hardness: The TE must survive direct FEL impact for energies up to 2mJ/pulse.
2. Dynamic range: The TE must be able to determine the total FEL energy over the full range from 1 μJ to 10 mJ, if necessary in conjunction with an attenuator for energies above 2 mJ.
3. Range of Validity: The extent to which the TE signal reflects the energy in the FEL fundamental shall be determined vs. photon energy, bunch charge, aperture, attenuator setting etc.
4. Absolute accuracy of pulse energy measurement: ± 10% at 10 mJ and within ± 25% at 10 μJ.
5. The absorbed fraction of the energy as a function of FEL photon energy shall be calculated.
6. The field of view is a circle with a diameter of 3 mm centered on the ideal FEL beam axis.
7. The sensor must be movable remotely by at least ± 5 mm about the nominal FEL beam axis.
8. Repeatability: At 200 μJ, measurements must be repeatable to ± 1%.
9. Speed: Measurement of the total FEL pulse energy for every pulse at rates up to 10 Hz is required, operation up to 120 Hz is desirable.
10. The TE must be remote-controllable into a configuration that does not obstruct the FEL radiation within the stay-clear zone defined by the Fixed-Mask clear aperture.
11. Periodic in-situ recalibration of the system sensitivity and energy calibration is required.

II. System Description

A. Basic Design Considerations

A thermal radiation sensor consists of an absorber optimized for the radiation of interest, a thermometer to measure the resulting change in temperature, and a thermal link to a reservoir that absorber and sensor can cool back down to. At LCLS, that radiation consists of a broad spontaneous background signal from the undulator, of which a small fraction at the fundamental energy produces the high-intensity FEL in the center though the process of self-amplified stimulated emission (SASE). The spontaneous background radiation spans an energy range up to ~400 keV with the total energy of ~20 mJ/pulse and is spread out over several cm^2, whereas the FEL signal at the fundamental lies between 800 eV and 8 keV with its total energy of ≤2 mJ concentrated in a small pencil beam with a Gaussian shape and a width between ~1 mm full-width at half maximum (FWHM) at 800 eV and ~0.2 mm FWHM at 8 keV.

The dimensions of the sensor in the TE are defined by the need that the output signal reflects the total energy of the FEL, with as small a contribution from the spontaneous undulator background as possible (requirements #3 and #5). It must therefore be thick enough to absorb essentially all of the FEL radiation up to the maximum FEL photon energy of 8 keV, while transmitting as much of the higher-energy spontaneous background as possible. The TE should also not be much wider than the 3 mm diameter field of view (requirement #6), since the FEL signal has a maximum spatial distribution of ~1 mm FWHM, while the spontaneous undulator background extends over many cm^2.

The absorber thickness is also determined by the absorber material, which in turn is determined by the need for the TE to be radiation hard, at least up to 2 mJ per pulse (requirements #1 and #2). Light low-Z compounds tend to be more radiation hard since they have longer absorption lengths and thus absorb less energy per volume (figure 1). Ideally, the absorber should also serve as the substrate to deposit the thermal sensor on, so that an epitaxial sensor film can be deposited onto it and the entire sensor can be made monolithic. The alternative of a separate absorber attached to the sensor through a comparably weak thermal link would slow down the cooldown and likely preclude operation at 10 Hz (requirement #9). This favors single crystal absorbers such as Si, SiC, sapphire (Al_2O_3) or possibly diamond (C).

B. Radiation Hardness

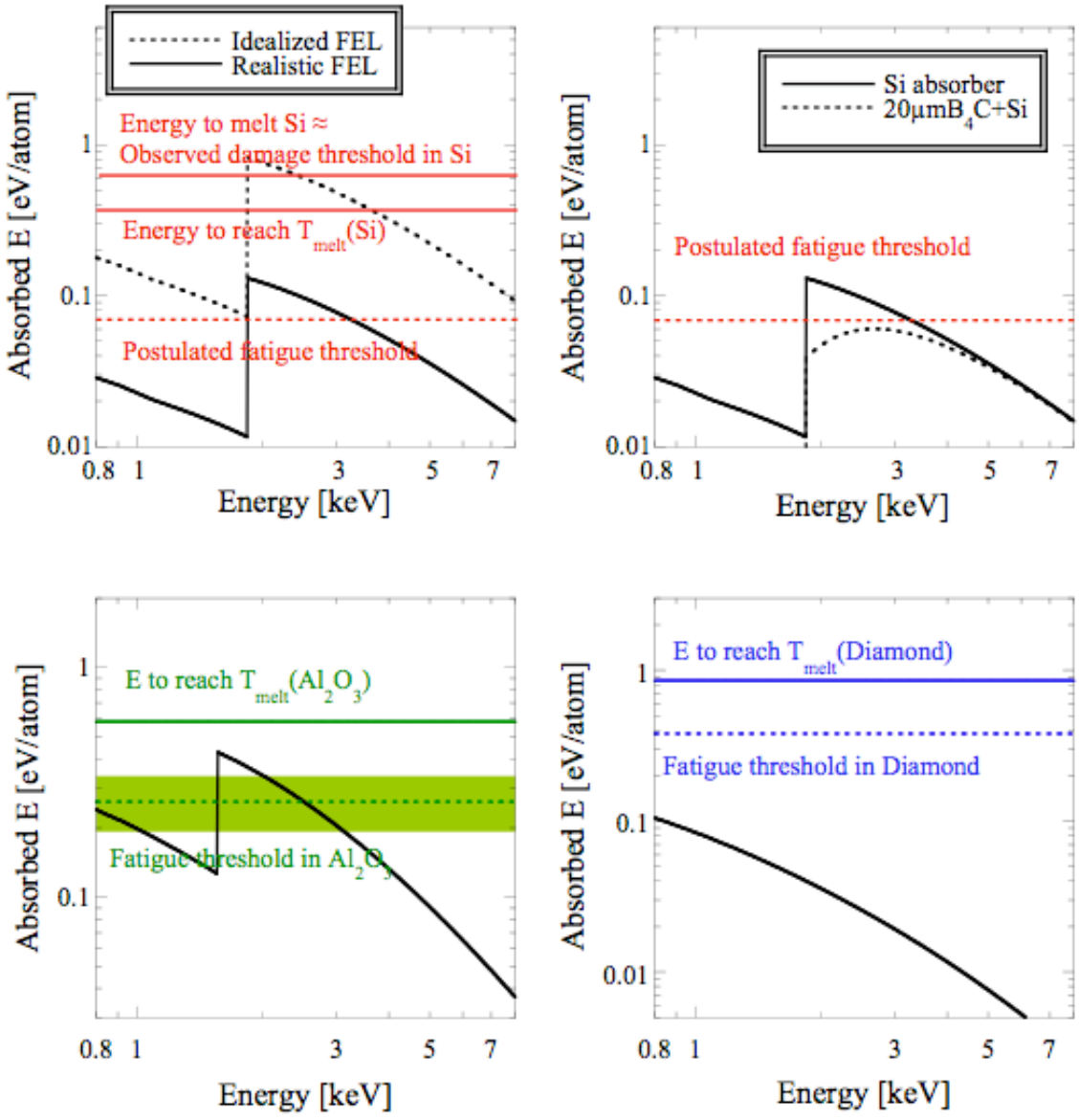

Figure 1: Peak energy deposition in a) Si (top left), b) Si with 20 μm of B_4C (top right), c) Al_2O_3 (bottom left) and 4) diamond (bottom right). Damage is expected to occur whenever the maximum deposited energy density exceeds the damage threshold of the material.

We have calculated the energy per unit volume that is deposited in different candidate absorber materials as a function of LCLS energy (figure 1). The LCLS beam is assumed to have a Gaussian shape with a width varying from 1 mm FWHM at 800 eV to 200 μm FWHM at 8 keV. It is absorbed over a material-specific absorption length [2], and the absorbed energy density peaks at the surface where the incident beam has the highest intensity. There is some uncertainty about the expected width of the FEL beam. Initial calculations of the FEL intensity have assumed an idealized uniform and homogeneous distribution of electrons in the electron bunch in the linac [3]. This produces a very narrow beam with correspondingly high fluence (figure 1a, dashed black line). Subsequent calculations assume randomly-distributed electrons in the bunch, which causes the beam to spread by a factor ~2-3 and reduce the fluence by a factor of ~4-9 (figure 1a, solid black line). We use the latter more realistic simulations as a basis for our calculations.

The absorbed energy density is to be compared to the damage threshold for different materials. We consider three different thresholds. The first is the absorbed energy density required to heat the absorber to its melting temperature, which is calculated using the temperature-dependent heat capacity of the materials. The second threshold takes into account the additional latent heat of condensation required to actually melt the material at the surface. This threshold is higher, and it agrees roughly with the damage threshold observed in tests on Si and other materials at the FLASH free electron UV laser facility in Hamburg, Germany [4]. Figure 1 shows that the deposited FEL energy does not exceed either threshold in Si, Al_2O_3 and diamond, provided the calculations of the wider FEL beam diameter are correct. This allows us to choose the absorber material for reasons other than just radiation hardness. Al_2O_3 was rejected because it is transparent for optical light, making energy calibration with an optical laser difficult. Diamond was rejected because is also transparent and because it is still too expensive for a development project. Si has the advantage of a huge literature on thin film processing on Si.

An additional fatigue threshold has been postulated due to the fact that the FEL duration is so short that the energy cannot dissipate quickly. When the thermal expansion upon heating causes the stress in the material to exceed its yield strength, the surface will start to become brittle and eventually crack after repeated exposure to the beam [5]. This fatigue threshold has not yet been observed experimentally, but could become important for the Si absorber of the TE in the energy range around ~2 keV above the Si K-edges where the absorption length is very short. Should this fatigue threshold turn out to be important for Si at LCLS, we can either deposit a ~20 μm boron carbide (B_4C) layer on the absorbing surface (figure 1b), or attenuate the incident beam with the gas attenuator.

We have chosen silicon as the absorber material for the total energy monitor at LCLS. The requirement to absorb at least 99% of the pulse at a maximum FEL energy of 8 keV, while absorbing as little as possible of the spontaneous halo in the higher-energy harmonics, suggests a thickness of the Si chip of ~400 μm. We have chosen a Si chip absorber with dimensions of 8 × 12 × 0.37 mm^3. This is large enough to over the field of view of 3 × 3 mm^2 (requirement #6), and have an area of several mm^2 at the edges to mount the Si chip to the detector stage for good thermal contact and thus fast cooldown. It is small enough to have several sensors side by side on the TE detector stage for redundancy in case one of them is damaged or the LCLS beam shows some unexpected characteristics. The sensor is placed on the back side of the Si chip to protect it from the FEL impact. The TE requirements of high dynamic range (#2) and a speed compatible with a FEL repetition rate of 10 Hz (#9) set the TE operating temperature.

C. Operating Temperature

The dynamic range and (more importantly) the speed requirements determine the operating temperature of the TE. Heat capacities C decrease with lower temperatures and therefore lead to larger temperature excursions $\delta T \propto E/C$ per absorbed energy E and thus higher sensitivity, which helps to extend the dynamic range to low pulse energies (requirement #2) and for an accuracy of ± 25% at 10 μJ (requirement #4). A lower bound to the heat capacity and thus the operating temperature is set by the need that the temperature excursion must not drive the sensor out of its linear range for high energy inputs. Thermal conductivities increase at lower temperatures because of reduced thermal phonon scattering, and therefore allow faster response times since the absorbed heat propagates faster through the Si chip and into the cryostat. This is important to make the TE compatible with an LCLS repeat frequency of 10 Hz (requirement #9).

We have performed finite element simulations of the sensor response to calculate the optimum operating temperature and device geometry. The simulation uses a 161 × 241 × 21 grid for the 8 mm × 12 mm × 0.37 mm Si absorber, with perfect coupling to the cryostat assumed at its two short edges and between the Si and the sensor. The LCLS signal is modeled as a Gaussian with a total energy E = 1 mJ and an absorption length of 1.5 μm corresponding to the absorption length in Si at the initial LCLS energy of 0.8 keV. The sensor is located at the opposite side of the FEL impact, with its center aligned with the center of the FEL beam. The temperature evolution is calculated by expanding the heat flow equation to first order, and propagating the temperature of each volume element in the grid according to the temperature differences to its six neighbors. The sensor signal is extracted by averaging the response over the sensor area, taking into account the temperature dependence of the Si heat capacity $C_{Si}(T)$.

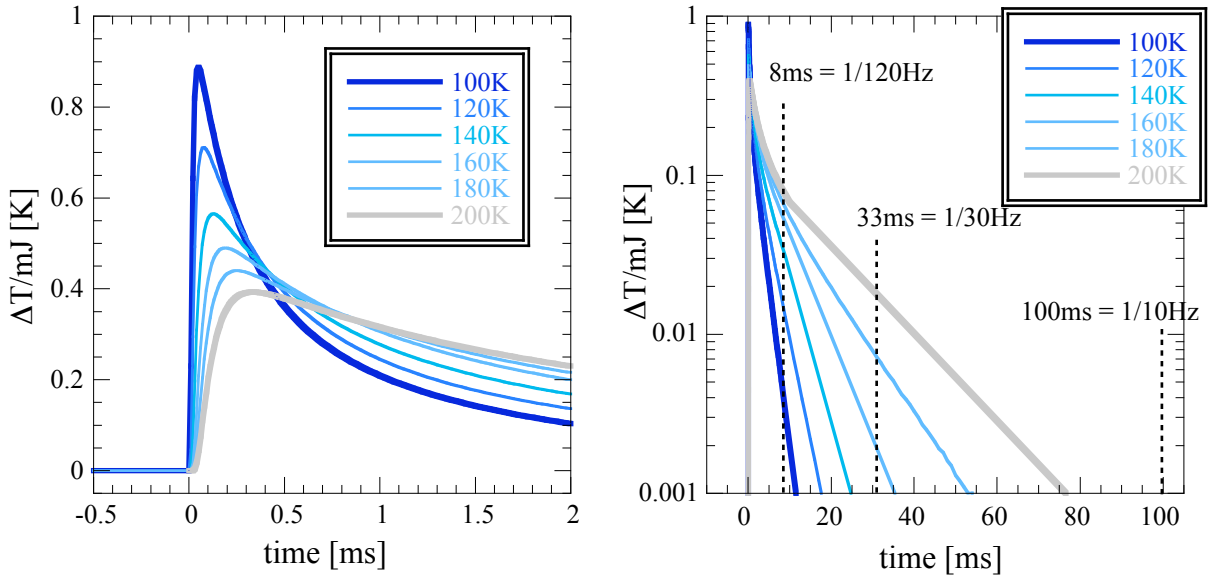

Figure 2 (left): Finite-element simulation of the thermal response of a 1 mm × 1 mm sensor on the back of a 370 μm thick Si absorber to an LCLS pulse of 1 mJ at 800 eV as a function of temperature. (Right): The same data plotted on a logarithmic scale for time scales up to 100 ms.

Figure 2 shows the simulations in the temperature range between 100 and 200 K. As expected, the signal amplitude increases at lower temperature where the Si heat capacity is lower.

The time scales for heat propagation through the Si substrate increase with increasing temperature due to the increased heat capacity and decreased thermal conductance. Assuming that the signal should have decayed to at least <1% of its peak value before the next FEL pulse is absorbed, figure 2b demonstrates that all sensor temperatures ≤200 K are compatible with an LCLS pulse frequency of 10 Hz, provided that the Si absorber chip is thermally well-coupled to the chip holder as assumed in the simulations. Operation at 120 Hz requires an operating temperature around ~100 K (requirement #9).

This suggests that the ideal TE operating temperature is around ~100 K. However, measurements of the response of prototypes have shown that Si-based sensors exhibit a prompt athermal signal in addition to the expected thermal signal (see discussion in section III). Since this prompt signal interferes with the thermal signal, it is necessary to wait until it has decayed before the thermal response peaks. This requires a TE operating temperature of ~180 K to slow down the rise time of the thermal signal. Operation at 180 K keeps the decay time sufficiently fast to be compatible with required 10 Hz operation, but probably not with operation at 120 Hz.

D. Device Geometry

The sensor size is set by a trade-off between sensitivity and susceptibility to beam jitter. Smaller sensors exhibit a larger signal amplitude, because the volume underneath the sensor that FEL energy has to spread over is smaller (figure 3 left). For the same reason, smaller sensors also have a faster rise time. On the other hand, the response of smaller sensors varies more strongly with beam jitter, because different fractions of the energy escape to the side if the FEL absorption location varies with respect to the location of the sensor (figure 3 right).

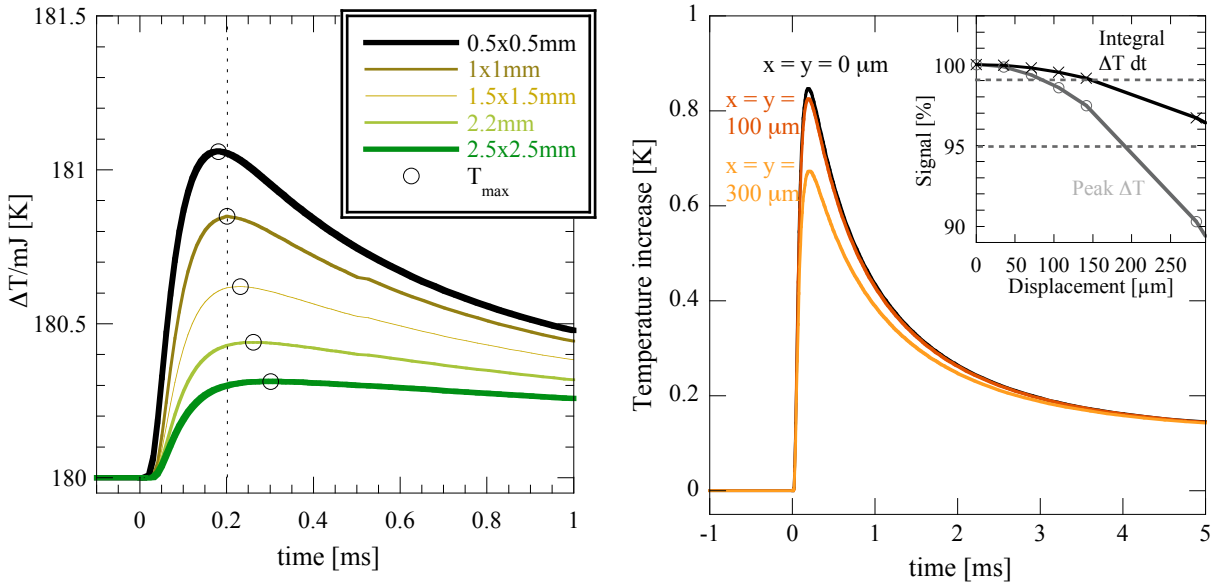

Figure 3 (left): Signal at 180 K for short time scales for different size sensors in response to an FEL energy of 1 mJ. The circles mark the time of the peak signals. (Right): Signal variations as a function of absorption location for a single-pixel device on a 3 × 3 mm^2 Si island device (see figure 4, bottom left). The displacement is measured relative to the center of the sensor. The inset shows that the variation in peak temperature (circles), are larger than the variations in the signal integrated to 10 ms (crosses) for the same amount of beam jitter.

A sensor area of 1 × 1 mm^2 is a good compromise between sensitivity and susceptibility to jitter, and is chosen as the baseline geometry for the TE (figure 4, top left). Further decreasing the sensor area will not increase the responsivity significantly (figure 3 left). On the other hand,

the signal variations are less than 1% for the integrated signal (2% for the peak signal) for the expected maximum beam jitter of ±10% of the beam width, i.e. ~100 μm at 800 eV. This is sufficiently insensitive to beam jitter to be compatible with the requirements for 10% accuracy. With this 1 × 1 mm^2 design, the responsivity of the TE is roughly ~1 K/mJ, as expected for silicon heat capacities of order ~1 $mJ/K/mm^3$ (figure 3 left).

One concern is that the beam jitter may exceed the calculated value, especially during the initial LCLS commissioning phase when the TE will primarily be used. If the increase in jitter is only moderately above the predictions, a single larger 2 × 2 mm^2 sensor will be appropriate (figure 4, top right), at the expense of reduced sensitivity by about a factor of ~2 (figure 3, left). For greatly increased jitter, or in cases some position resolution is desirable, five-pixel devices will be fabricated (figure 4, bottom left). The ratio of the signals in the left to the right column provides horizontal position information, the ratio of the signals in the top to the bottom row provides the vertical coordinate of the FEL centroid. Single pixel and five-pixel devices can be placed on a 3 × 3 mm^2 Si island that is suspended by eight 0.1 × 0.2 × 0.1 mm^2 Si bridges (figure 4 bottom row). In this design the island heats up uniformly before the cooldown through the thermal bottleneck, and variations in absorption location are washed out (figure 3, right)

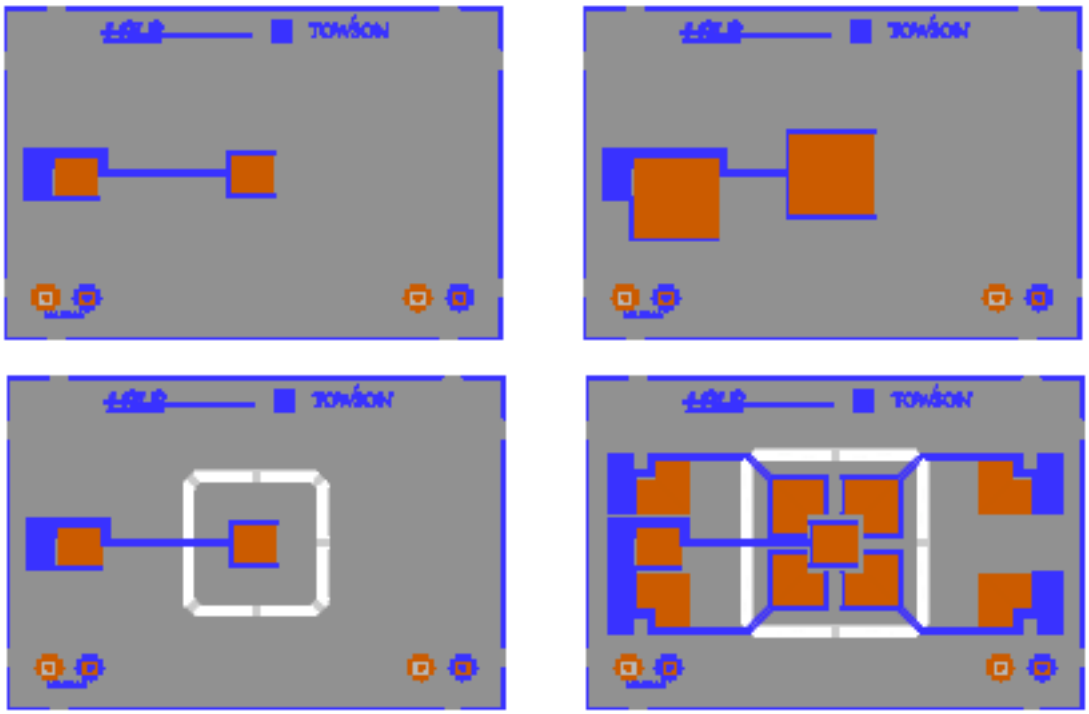

Figure 4: Sensor mask layouts. Top left) Single small 1 × 1 mm^2 sensor for high sensitivity (basic design). Top right) Large 2 × 2 mm^2 sensor for situations with increased beam jitter. Bottom left) Single pixel sensor on 3 × 3 mm^2 island suspended by eight 0.1 × 0.2 × 0.1 mm^2 Si bridges. Bottom right) Five-pixel device with spatial resolution on 3 × 3 mm^2 island for situations with unexpectedly large beam jitter. Each sensor is accompanied by an identical resistor on the side of the wafer outside the FEL beam path to complete the bridge circuit of the preamplifier readout.

E. Sensor Materials

Given the multitude of possible sensor materials and the desire to retain some design flexibility, we decided early on to base the TE sensor on rare-earth manganites. They have the general composition $(RE)_{1-x}(EA)_xMnO_3$, where RE is a rare earth and EA is an earth alkaline element. They have a sharp metal-insulator transition with resistance changes as high as >10%/K over a range of several Kelvin (figure 5). This is sufficiently sharp to have high sensitivity for low energy input and sufficiently wide to offer a large dynamic range (requirement #2 and #4). Importantly, the transition temperature of the rare-earth manganites can be adjusted over a wide range of temperatures though the choice of the specific RE and EA elements, through their ratio x, and through details of the deposition conditions. These materials have attracted great interest over the last decade because the transition temperature also changes with magnetic field, giving rise to their classification as "colossal magneto-resistive" (CMR) materials. Significant effort has been made to grow these materials on Si wafers for use in the semiconductor industry, and although their development for thermal sensors is less common, the information for CMR film growth and characterization is available.

For bolometers with a transition temperature between ~100 and ~200 K, neodymium strontium manganese oxide (NSMO) is an appropriate choice [6]. For the TE a composition of $Nd_{0.67}Sr_{0.33}MnO_3$ was chosen, which can be deposited on buffered Si substrates by pulsed laser deposition (PLD). The buffer layer is required to prevent chemical reactions and to overcome lattice and thermal expansion mismatch between NSMO and Si. In addition to the material choices, other parameters play an important role in determining the properties of thin films grown by PLD, such as [6]:

- Laser energy density (determined by the pulse energy and spot size)
- Substrate temperature during film growth
- Partial pressure of the ambient gas during growth
- Oxygen partial pressure during cool down
- Temperature ramp rates during the heating and cooling steps

These parameters were optimized by our collaborators at Towson University (Prof. Rajeswari Kolagani's group) to grow $Nd_{0.67}Sr_{0.33}MnO_3$ (NSMO) films to be used as sensors in the Total Energy Monitor at LCLS. Initially, only an strontium titanate ($SrTiO_3$, STO) buffer grown at Motorola Laboratories by molecular beam epitaxy (MBE) was used [7], and the NSMO was deposited with the substrate held at a temperature of 770°C in an atmosphere of 400 mTorr of N_2O. This produces slightly oxygen-deficient films for TE operation at a temperature of T ~ 100 K (figure 5, left). After observing the fast athermal artifacts in the sensor response, which necessitated a higher operating temperature (see section III), the buffer layers were changed to STO plus bismuth titanate ($Bi_4Ti_3O_{12}$, BTO). This secondary buffer reduces the strain in the NSMO, which is now deposited by PLD at an increased temperature of 790 °C and cooled down at a higher oxygen pressure of 500 Torr. This produces sensor films that are not oxygen-deficient and whose metal-insulator transition peaks at a temperature of ~200 K, closer to the temperature of bulk NSMO (figure 5, right) [6, 8]. Finally, STO was replaced by yttrium-stabilized zirconia (YSZ) and cerium dioxide (CeO_2) buffer layers, so that we no longer depend on the availability of Motorola's STO deposition process by MBE, while maintaining an operating temperature of ~180 K and a high temperature coefficient of resistance $TCR \equiv 1/R\ \partial R/\partial T \approx 10$ %/K. A detailed description of the NSMO sensor fabrication by pulsed laser deposition is given in a separate ESD, *Total Energy CMR Production*, ESD 1.5-108.

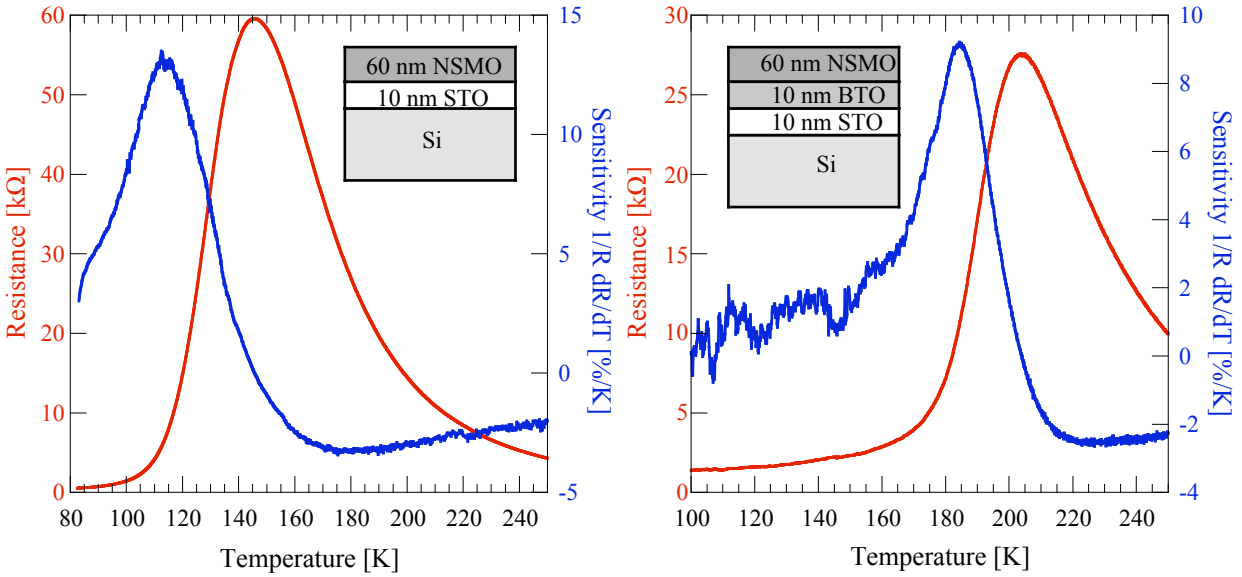

Figure 5. Schematic design of different implementations of the total energy monitor, optimized for different regimes (insets, not to scale). In every case, the 375 µm Si substrate serves as the radiation absorber and as the substrate for growth of the NSMO sensor film. (Left) Resistive transition of $Nd_{0.67}Sr_{0.33}MnO_3$ grown on a 10 nm STO buffer for operation at ~100 K. (Right): Resistive transition of $Nd_{0.67}Sr_{0.33}MnO_3$ grown on a 10 nm STO plus 10 nm BTO buffer under conditions optimized for operation at ~180 K.

The sensor dimensions (red in figure 4) are defined photolithographically with a room temperature acid etch in a solution of potassium iodide (KI) and 10% hydrochloric acid (HCl). The sensor is contacted with a 200 nm Au wiring layer that is deposited by magnetron sputtering, and photolithographically defined by lift-off (blue in figure 4). To ensure proper adhesion of the Au to the Si, the Si chip is first cleaned for 30 s by ion milling in argon, and a 30 nm Ti layer is deposited immediately before Au sputtering. Thicker Ti adhesion layers affect the R(T) curve of the NSMO sensor, typically apparent as an increased resistance at low temperature that is likely due to an oxygen-depleted NSMO surface layer where the Ti forms TiO_2. Thinner Ti layers lead to unreliable Au adhesion, with parts of the Au wiring delaminating from the Si chip during lift-off. Future devices might consider replacing the Ti with a Cr underlayer since Cr reacts less strongly with oxygen and is therefore expected to degrade the interface layer less.

When this detector is biased at a voltage $V = RI$, the signal in response to a temperature increase ΔT due to absorption of an LCLS pulse is given by [9]

$$\Delta V_{out} = \frac{\partial V}{\partial R}\frac{\partial R}{\partial T}\Delta T = V \cdot TCR \cdot \Delta T, \qquad (1)$$

where TCR ≡ 1/R ∂R/∂T is the temperature coefficient of resistance, a measure of the steepness of the resistive transition and thus the device sensitivity with a value of ~10 %/K according to figure 5. For a bias voltage of 1 V and a typical responsivity of 1 K/mJ according to figure 3, the peak output signal is of order ~0.1 V per mJ of energy input. Since the TCR is constant to within a few percent over a temperature range of several Kelvin, this sensor fulfills the requirements of a dynamic range up to 2 mJ, with extensions to 10 mJ possible if a small non-linearity in the response due to the non-linearity of the TCR is acceptable (requirement #2).

F. System Overview

An overview of the total energy monitor (TE) system is given in figure 6. The NSMO sensor on the Si absorber is held in the LCLS FEL beam path inside a UHV sample chamber. It is held by a copper stage attached to a pulse tube cryostat that allows cooling the NSMO sensor to a desired operating temperature. The cryostat is supported by an xyz-stage so that it can be moved by at least ± 5 mm about the nominal FEL beam axis to align it with the actual FEL position (requirement #7). The xyz-stage has a vertical travel of 8" so that the TE can be withdrawn upwards to clear the LCLS beam path (requirement #10). In the withdrawn position, the TE faces an optical calibration laser for periodic in-situ recalibration (requirement #11). The calibration laser and the optical components to attenuate, characterize and focus it onto the TE are placed on a small optical table to the side of the FEL beam path. The individual subsystems are discussed in the following sections.

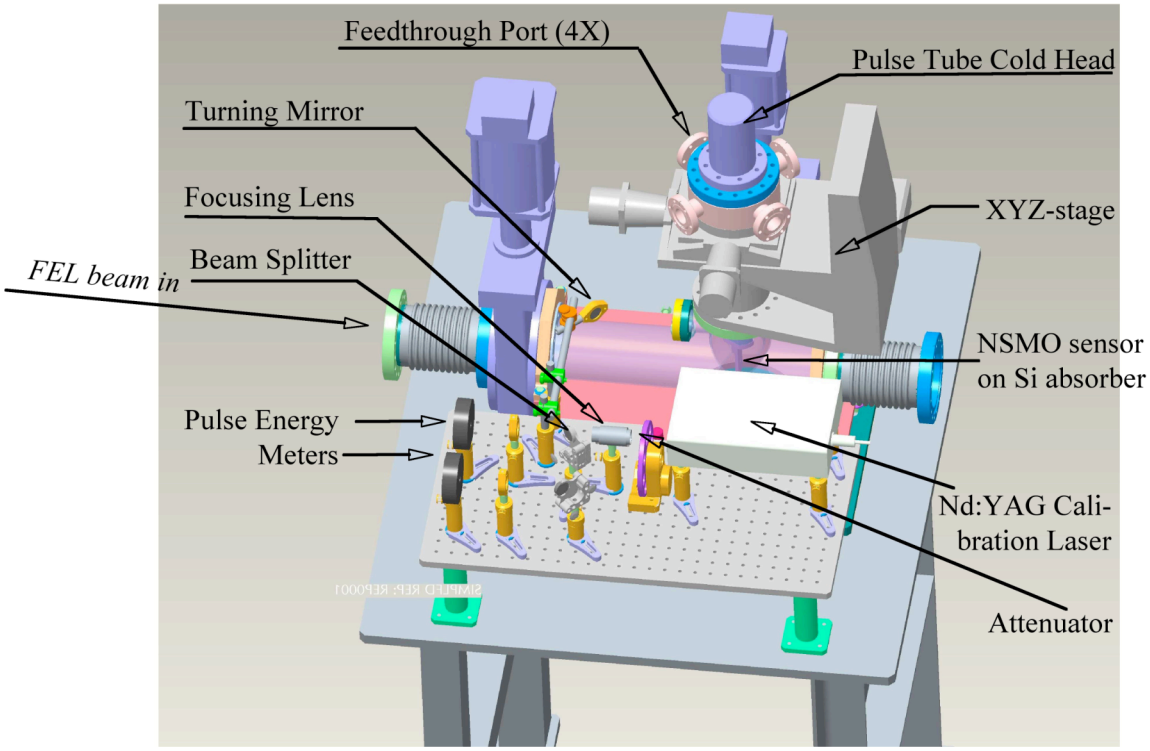

Figure 6: Total Energy Monitor, system overview.

G. Subsystems

G1. Mechanical and Vacuum

The total energy monitor (TE) will be integrated into the LCLS FEL beam path with a custom-designed vacuum chamber. The chamber is separated from the neighboring beam line by large gate valves and has its own turbo pump (not shown) and ion pump (figure 7 left) so that it can be brought to atmosphere independently from the rest of the LCLS. Standard pressure gauges for operation down to a base pressure of ~10^{-7} Torr and safety features such as burst disk and a laser enclosure will be installed.

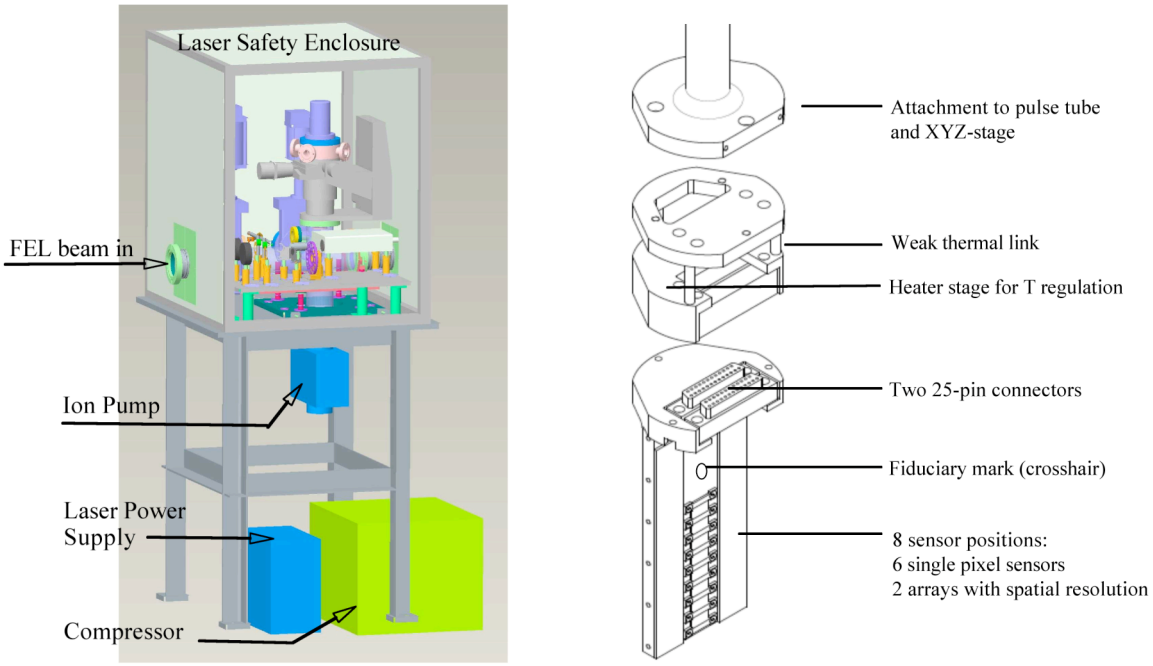

Figure 7 (left) TE system with vacuum components and laser safety enclosure. (Right) The Cu TE sensor holder can hold up to 8 Si chips for a total of 16 pixels (6 single-pixel devices and two 5-pixel arrays). It contains a resistive heater and is suspended off the refrigerator through a weak thermal link to allow regulation of the sensor temperature above the refrigerator base temperature.

The NSMO sensor chip is mounted to an oxygen-free high conductivity (OFHC) Cu block. Up to 8 sensor chips can be mounted simultaneously so that spare sensors are available in case the initial sensors are damaged or the LCLS beam shows unexpected characteristics. The sensor chip mount and the cryostat are supported by an xyz-stage so that they can be moved by at least ± 5 mm about the nominal FEL beam axis to align it with the actual FEL position (requirement #7). We have chosen the xyz-stage model # 678044, fabricated by MDC Vacuum, because it can be equipped with standard stepper motors and allows fine positioning with 3 µm per step in x and y and 5 µm per step in z. This xyz-stage has ±0.5" travel in the horizontal directions and a full range of 8" travel in vertical direction so that the TE can be withdrawn upwards to clear the LCLS beam path (requirement #10). In the withdrawn position, the TE faces an optical calibration laser for periodic in-situ recalibration (requirement #11).

G2. Refrigeration

It is highly desirable to cool the TE to its operating temperature in the LCLS tunnel without the use of liquid cryogens. Since conventional mechanical cryocoolers produce significant vibrations, which can couple into the readout electronics and increase the electronic noise contribution, the need for high dynamic range down to 1 µJ/pulse (requirement #2) and good reproducibility (requirement #8) favor the use of a pulse tube refrigerator. These mechanical cryocoolers exhibit significantly lower vibrations, because the vibrating rotary valve that separates the high and low-pressure regions can be physically removed from the vacuum chamber that houses the TE.

We have chosen a 70 K pulse tube refrigerator from VeriCold Technologies (figure 8 right), whose rotary valve is connected to the vacuum chamber only through a single ~3 m long ¼" Cu tube. This cryocooler has a base temperature <60 K and cooling power of 3 W at 70 K,

more than sufficient for the heat load of the 16 × 3 = 48 signal wires plus the radiative heat load from 300 K. Its low-frequency vibrations are below 20 μg/√Hz, where g = 9.81 ms^{-2} is the standard acceleration of gravity. For temperature stability and flexibility in the operating temperature, the TE detector stage is not connected directly to the cold head of the pulse tube, but suspended off the cold head through a weak thermal link so that the detector stage can be heated and be regulated at the desired operating temperature (figure 7 right). A standard platinum thermometer, model PT100, and a modern PID temperature controller, Model 340, fabricated by Lakeshore Cryogenics, are appropriate for temperature regulation between ~100 and ~200 K with an accuracy of a few mK over many days (figure 8, left).

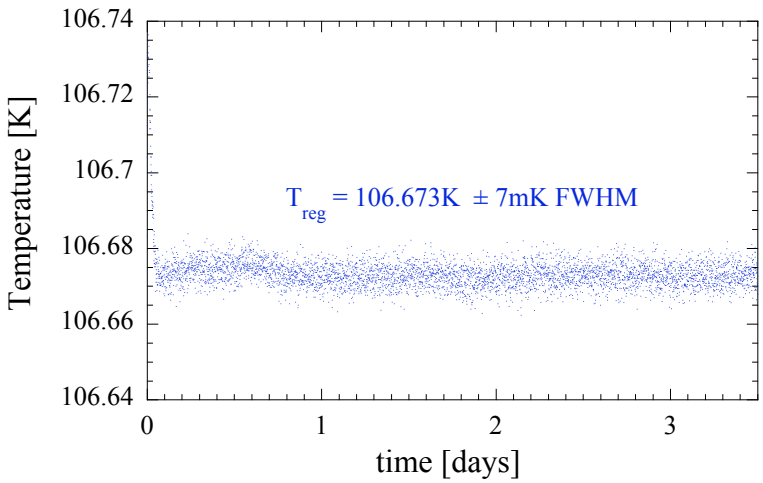

Figure 8 (left):Picture of the 70 K pulse tube, mounted onto a standard 4 ½" CF flange. The cold head that connects to the TE detector stage is at the bottom of the pulse tube, and the gas inlet on the top right-hand side of the instrument is the connection to the rotary valve and the compressor. (Right) The temperature stability of the TE detector stage over a period of >3 days for regulation at T = 106.673 K. Temperature variations of <10 mK FWHM

G3. Read-Out Electronics

The preamplifier readout for the TE is based on a dc-coupled balanced bridge circuit. It employs a AD8138 differential op-amp with an input voltage noise of 5 nV/√Hz, comparable to the Johnson noise $(4k_BTR)^{1/2} \approx 7$ nV/√Hz of the NSMO sensor itself. The preamplifier applies a bias voltage of 2 V across the NSMO sensor, producing a peak signal of 200 mV per mJ of input energy according to equation (1), i.e. roughly 200 μV for the minimum energy input of 1 μJ. The preamplifier noise is sufficiently low to enable a signal-to-noise ratio of >100 at the minimum LCLS energy. It fulfills the requirement of a dynamic range down to an LCLS energy of 1 μJ per pulse (requirement #2). It is also more than sufficient for an absolute accuracy of pulse energy measurement of ± 10% at 10 mJ and ± 25% at 10 μJ (requirement #4), and for a repeatability of the energy measurement to ± 1% at 200 μJ (requirement #8). The preamplifier design is described in detail in a separate ESD, *Total Energy Monitor Electronics*, ESD 1.5-107.

G4. Calibration Laser

A pulsed optical laser is used to calibrate the response and the linearity of the total energy monitor in-situ (requirement #11). The laser must meet the following requirements. Its energy per pulse must cover the full range between 1 μJ and 2 mJ per pulse (requirement #2), ideally up to 10 mJ in case future upgrades further increase the LCLS pulse energy (requirement #4). The fluctuations of the energy output should be well below 10% between pulses so that they do not

contribute substantially to the TE calibration error. The pulse length should be short compared to the thermal time constants of the TE in the microsecond range so that it resembles the fast energy deposition for this thermal device, although it does not necessarily have to be as short as the FEL pulse duration of ~200 fs. The laser repeat frequency should be compatible with the LCLS repeat interval of 100 ms during setup when the TE will mostly be used for cross-calibration of other instruments. Operation at 10 pulses/s is therefore required, and while operation at 120 pulses/s is desirable, it is not essential.

The laser wavelength is chosen so that a) it can be transmitted into the vacuum chamber without too much loss in the vacuum window and b) it is mostly absorbed in the total energy monitor. For enhanced safety during setup, an optically visible laser is strongly preferred over a UV or IR laser. Optical wavelengths also turn out to be the wavelength range favored by absorption requirements, since UV lasers tend to have a shorter absorption length than X-rays and therefore lead to radiation damage in the TE at energies less than the maximum LCLS pulse energy, and IR radiation tends to have longer absorption lengths than X-rays and therefore is not fully absorbed in the TE (figure 9). The laser spot size must allow focusing the calibration pulse to a diameter comparable to the diameter of the LCLS FEL, which varies between ~1000 µm FWHM at 800 eV and ~200 µm FWHM at 8 keV. Secondary considerations for choosing a calibration laser include its physical size, cost, and ease of remote operation.

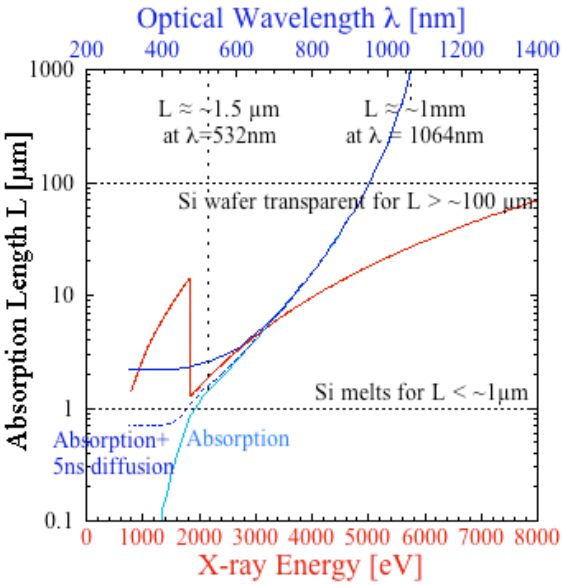

Figure 9: Absorption lengths for optical and X-ray photons in Si.

These requirements make lasers at 532 nm a good choice for TE calibration. The light falls into the green visible range, its absorption length of ~1.5 µm in Si is comparable to the absorption length of the 800 eV photons that the LCLS FEL will be run at initially, and it can be produced comparably easily with a frequency-doubled neodymium-YAG laser.

We have chosen a Minilite-I laser, fabricated by Continuum, as the calibration laser for the TE. It produces 5 ns pulses in a 3 mm diameter spot with a maximum repeat frequency of 15 Hz. The frequency-doubled output at 532 nm has a maximum energy of 12 mJ/pulse, with fluctuations of the energy output of 1% rms (3% peak-to-peak for 99.9% of the pulses). The Minilite can be remotely triggered with 5V TTL pulses for remote-controlled activation. Its energy can be adjusted to cover the full LCLS energy range with an external remote-controllable

attenuator. Less than 0.05% of the energy is at the fundamental laser wavelength of 1064 nm. The small size of the laser (~27 × 17 × 7 cm) allows it to be placed inside the radiation enclosure, and the power supply (38 × 20 × 36 cm) can be placed under the support table of the TE. The cost of ~$14k is comparably low for a pulsed Q-switched laser.

(As an aside, TE calibration with an electrically-pulsed resistor was considered and tested, but quickly rejected. The thermal coupling between the resistor and TE absorber is too weak to enable fast energy deposition. And even if the thermal coupling could be improved, it is unlikely that the calibration resistor could be placed at the exact impact location of the LCLS FEL, because of radiation damage it would experience. Therefore, such electrical calibration would suffer from uncertainty due to a difference in heat flow geometry.)

G5. Optical Calibration System

The optical calibration system attenuates the pulsed output from the calibration laser to the desired energy and focuses it onto the TE while the sensor is withdrawn from the FEL beam path. The system measures 1) the incident pulse energy, to calibrate the response of the TE, and 2) the reflected pulse energy, to monitor potential damage to the TE surface from exposure to the FEL.

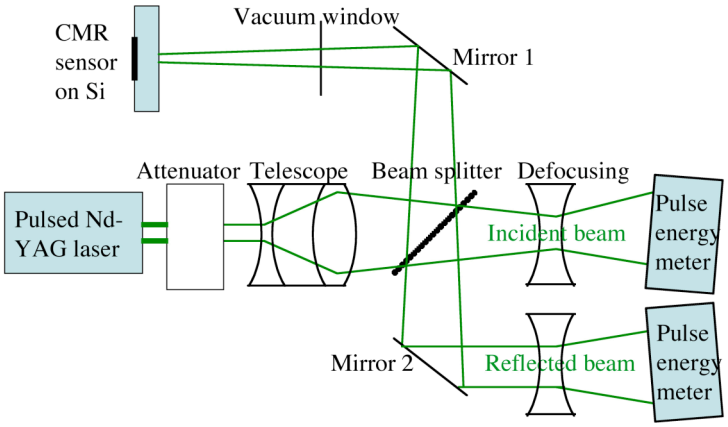

Figure 10: Schematic of the optical setup for TE calibration

Figure 10 shows the optical path of the pulsed laser. The attenuator consists of a polarizer-analyzer and is placed directly after the laser output to protect the subsequent optical components. After the attenuator, a telescope focuses the laser beam onto the back side of the TE, with its focal lengths adjusted to produce a spot size of the desirable diameter, around ~1 mm. The telescope initially expands the incident beam to reduce its energy density and thus prevent damage to the subsequent optical components.

A beam splitter deflects a well-defined fraction, in the simplest case 50%, of the beam towards the TE while letting the remainder pass onto a pulse energy meter to monitor the energy of the incident beam. We have selected pyroelectric PE-10 pulse energy meters, fabricated by Ophir, since they cover the entire range of FEL energies from 2 μJ to 20 mJ/pulse. A defocusing lens is placed in front of the pulse energy meter to keep the intensity of the beam below the damage threshold of the meter. The meter is slightly rotated to prevent the beam from being reflected into the laser or the secondary meter.

The other half of the beam, after the beam splitter, is deflected onto the sensor through a mirror. This mirror is placed above the LCLS FEL pipe, to keep the entire optical setup on one small optical table on one side of the beam pipe and so simplify alignment. The vacuum window

is anti-reflection (AR) coated SiO_2, for high transmission at 532 nm. It is placed further away from the sensor, closer and to the mirror, where the diameter of the calibration beam is larger, to reduce damage to the AR coating during calibration. At 532 nm, only ~37% of the beam is absorbed in the Si substrate. The rest is reflected, and the intensity of the reflected beam is monitored with a second pulse energy meter. The role of this secondary meter is to monitor the ratio of incident to, reflected beam to assess the quality of the absorbing Si surface remotely, since FEL radiation damage to that surface is likely going to change the reflection properties of the Si surface. The beam splitter and the two mirrors are mounted on gimbal mounts, to aid alignment of the beam onto the sensor.

H. Error Budget

We briefly summarize the limiting errors that determine the accuracy of the total energy monitor:

- Energy calibration errors: <3%
  Set by the absolute accuracy of the PE-10 pulse meters (according to the manufacturer's specifications) that are used to measure the energy of the optical calibration laser.
- Electronic noise error: <<0.1% at saturation, <5 % at low energies
  Set by the electronic noise of the preamplifier readout and the NSMO sensor signal and noise characteristics. Although the electronic noise contribution is calculated to be <1%, even at low LCLS energies, according to section G3, a high 1/f noise contribution from the NSMO sensor or a reduced signal height could increase that error to several percent.
- Energy loss error: <2%
  About 2% of the FEL X-ray energy escapes the Si substrate in the form of high-energy electrons. This error can be calculated and compensated.
- Jitter error: <2%
  The beam jitter is expected to be ±10% of the beam width, i.e. between 100 µm at 800 eV and 20 µm at 8 keV. This can cause an error up to 2% according to figure 3, unless the beam jitter is unexpectedly large.

Adding these independent errors in quadrature, the total error in the accuracy of the measurement varies between < 4 % at an LCLS saturation energy of 2 mJ/ pulse, and <7% at low LCLS energies of 10 µJ/pulse. It is likely dominated by the accuracy of the pyroelectric pulse energy meters that measure the energy of the optical laser that the TE calibration is based on.

III. Preliminary Results

A. TE with an Operating Temperature of 100K

A prototype total energy monitor has been built according to the above specifications [10]. An NSMO sensor on a Si substrate with a maximum TCR = 12 %/K at T = 110 K (figure 5, left) was mounted in the prototype chamber and cooled to 110 K. It was illuminated at a rate of 10 Hz with a pulsed Nd-YAG Minilite-I laser that has been frequency-doubled to a wavelength of 532 nm. Its output was adjusted between 20 nJ and 12 mJ per 5 ns pulse to cover the energy range of interest at LCLS.

The response of the total energy monitor at T = 110 K to pulsed optical laser light is shown in figure 11 (left). In addition to the thermal signal expected according to figure 2, a significantly larger prompt signal is observed that overlaps with the thermal signal and affects a measurement of the thermal response. Surprisingly, this prompt signal is observed even at V_{bias} = 0 where any thermal signal is expected to be zero according to equation (1) [9]. In addition,

while the amplitude of the prompt signal changes with V_{bias}, it does not increase linearly with V_{bias}, and it increases roughly logarithmically in some devices with pulse energy, neither of which is expected for thermal devices. Actually, the prompt signal does not depend on the presence of an NSMO sensor at all, i.e. it is not of a thermal origin. For these reasons, it cannot be used as an alternative measure of the pulse energy. The prompt signal can change polarity, sometimes as function of temperature or as a function of absorption location, and its magnitude is often irreproducible between nominally identical devices. Control experiments on metallic aluminum samples do not exhibit any fast transients, suggesting that the prompt signals are fundamentally related to the characteristics of the semiconducting absorber material.

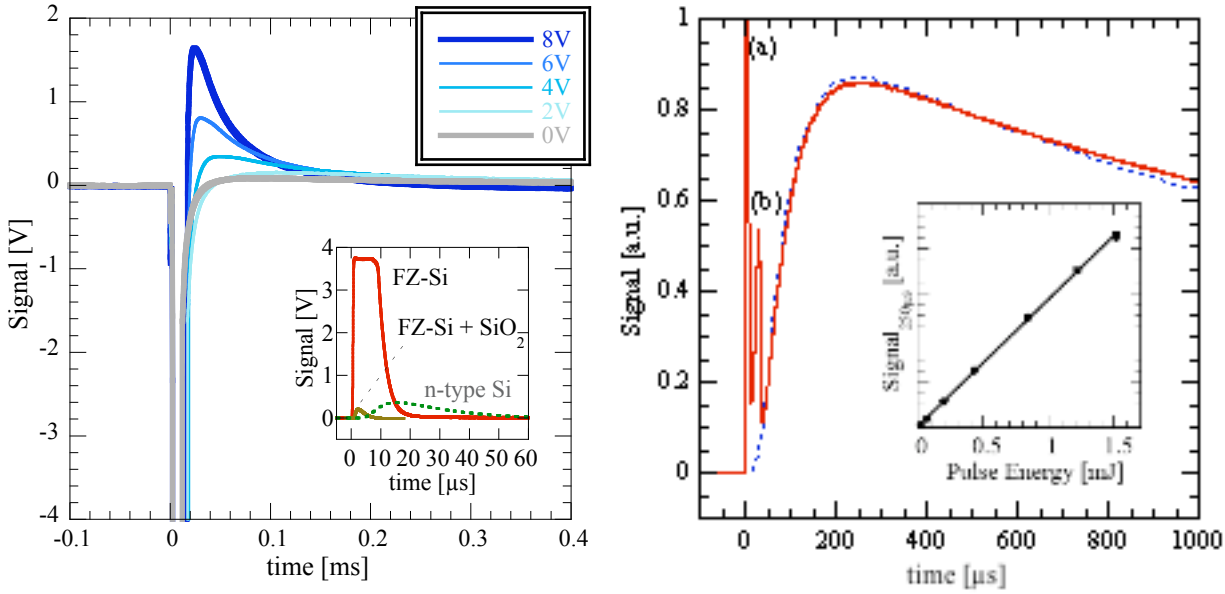

Figure 11 (left): Photoresponse of the bolometer of figure 5 (left) at T ≈ 110 K for different bias voltages. Note that there is a strong prompt signal at V = 0, and that the amplitude does not scale linearly with bias. The inset shows the response to 20 nJ pulses for test devices consisting of just an Au bond pad (no NSMO sensor at all) on float-zone (FZ) and doped (n-type) Si substrates. (Right): Photoresponse of the thermal sensor of figure 5(right) at T = 185 K. Note that the prompt signals, i.e. the Dember voltage (a) and the transient thermoelectric voltage (b), have decayed by the time the thermal signal reaches its peak. The pulse shape of the measured thermal signal (solid red line) is in good agreement with the calculations (dashed blue line). The inset shows that the peak signal at t = 250 µs scales linearly with the incident laser energy.

We have fabricated several test structures without NSMO films to investigate the origin of the prompt transients [10]. These test structures typically consisted of a Si substrate (p-type, n-type, or high-purity float zone Si), sometimes with a buffer layer (STO, SiO_2 or yttrium-stabilized zirconia YSZ), and a single ~1 mm^2 Au bond pad from where the connection to the input of the preamplifier was made. Initially, the change of polarity in the earliest sensors at T ≈ 120 K pointed towards a possible piezoelectric origin, since STO is piezoelectric and the thermal expansion coefficient of Si changes polarity at ~120 K. A piezoelectric origin of the prompt signal was eventually ruled out for several reasons:

- The presence of the prompt signal does not depend on the presence of an STO buffer film, and Si by itself is not piezoelectric. The prompt signal does not exhibit a polarity change at 120 K in all Si devices.

- The magnitude of the prompt signal is suppressed by several orders of magnitude when piezoelectric SiO_2 is placed between the Si and the Au bond pad. The inset in figure 11, left, shows that the prompt signal in response to the minimum laser energy of 20 nJ/ pulse already saturates the amplifier output in a high-purity float-zone Si chip, while a neighboring test device from the same Si chip with an additional SiO_2 layer tested during the same run under exactly identical conditions showed a much smaller prompt signal.
- Test structures with thin YSZ buffers consistently showed a larger prompt signal that those with thicker YSZ.

These observations point towards an electron-mediated origin of the prompt signal, albeit one that must be consistent with transient observations at $V_{bias} = 0$. It is unlikely that the formation of a pn-junction in the Si and charge separation due to the intrinsic field of the associated depletion layer can fully account for the prompt signal:

- The prompt transients are observed in test structures on highly-doped Si where the depletion layer is at most a few microns thick and located on the opposite site of the laser impact. Electron-hole pairs generated by the absorption of the 532 nm laser within a few μm of the Si surface will not experience any field until they have diffused into the space charge region.
- While the prompt signal is faster in high-purity float-zone (FZ) Si than in doped Si (inset figure 11, left), it is not necessarily bigger, although the space charge region should be much larger and the recombination time much longer in FZ Si and should therefore capture more electron hole pairs before recombination.

We believe [10] that there are two mechanisms that likely account for the observed prompt transients. One is due to the different mobilities of electrons and holes in Si, which causes them to separate during diffusion along the concentration gradient in the Si absorber after non-uniform illumination (Dember effect) [11, 12]. Since electron mobilities are higher than hole mobilities in Si, the laser-absorbing surface charges up positively, generating an observable voltage until the electrons and holes either recombine or are distributed evenly throughout the Si. This process depends not only on the relative mobilities of the electrons and holes in Si, but also on the relative velocity of their recombination at surface states. This can lead to a polarity reversal of the Dember voltage when front-surface recombination of the holes is faster than the back-surface recombination [12]. This depends on details of the surface treatment and therefore varies sensitively with sensor preparation. The magnitude of the Dember effect is non-linear with laser energy since a high density of electron-hole pairs can produce a Dember voltage large enough to drag holes along with the faster electrons, and thus prevent charge separation until the electron-hole density (and thus the Dember voltage) has decreased significantly from its initial value. Insulators, including piezoelectric buffers, reduce the coupling between the Dember signal and the Au bond pad.

The second effect responsible for fast transients is consistent with the diffusion of thermally generated majority carriers in the Si substrate from higher to lower temperature regions (transient thermoelectric, or Seebeck effect) [11, 13]. The polarity of this effect depends on the polarity of the majority carriers in the Si, i.e. positive for n-type and negative for p-type doping. The transient thermoelectric signal decays with a characteristic carrier recombination time or the time for temperature equilibration within the Si chip, whichever is shorter.

B. TE with an Operating Temperature of 180K

The easiest way to address the interference of the prompt transients with the thermal response of the NSMO sensor is to slow down the thermal signal such that it peaks at a time when the two prompt signals have decayed to zero. This is possible by fabricating NSMO sensors with a higher transition temperature, because the thermal response at ~180 K reaches its maximum only after ~250 µs (figure 2). To avoid having to slow down the thermal signal to the point that it is no longer compatible with the required operating frequency of 10 Hz, it is helpful to speed up the prompt transients as much as possible. This is accomplished using high-purity float-zone Si with a resistivity >10 kΩcm as a starting material (see inset figure 11, right). The fabrication of NSMO sensors for an operating temperature of 180 K is outlined in section II.E and in more detail in the separate ESD 1.5-108, on NSMO thin film deposition. A representative R(T) curve of such a sensor is shown in figure 5 (right).

The sensors were mounted in the prototype chamber, cooled and temperature-regulated at 185 K where they exhibit the highest sensitivity (figure 5, right). They were illuminated by the Minilite-I pulsed optical laser with an energy between 20 nJ and 2 mJ per 5 ns pulse. Figure 11 (right) shows the response of the sensor to 1 mJ pulses of the 532 nm calibration laser. As expected, according to figure 2, the thermal signal is greatly slowed down compared to sensors operated at T = 110 K, with the thermal signal reaching its maximum value only after $t \approx 250$ µs. In addition to the thermal signal, the two prompt transients are clearly visible. The Dember voltage (a) is very fast in the high-purity Si absorber and sufficiently strong to saturate the preamplifier output. The preamplifier has a recovery time of ~5 ns, and is therefore fast enough to record the somewhat slower transient thermoelectric signal (b) that peaks after ~40 µs. Most importantly, both prompt transients have fully decayed to zero by the time the thermal signal reaches its maximum. The amplitude of the thermal response at t = 250 µs is therefore linear with the incident laser energy over the entire energy range of interest for LCLS (inset figure 11, right). The prototype therefore fulfills the requirement of a dynamic range up to 2 mJ/ pulse (requirement #2), and can be calibrated in-situ over that energy range (requirement #11).

Note that the signal shape of the thermal signal agrees very well with the finite element calculations for short time scales (dashed line). However, for longer time scales the signal does not yet decay as quickly as predicted. After 100 ms, the thermal signal has only decayed to ~3% of its peak value, indicating that the thermal coupling of the Si chip to the OFHC sample holder through the In contact should be improved for LCLS operation at 10 Hz during commissioning. Also, the amplitude of the thermal signal is about a factor 4 smaller than expected. This is likely due to the formation of a diode-like structure at the interface between the sensor and the buffer layer, and the subsequent partial shunting of the signal through the substrate. We have measured the signal at 180 K at different bias voltages, and observe a bias-dependent decrease in CMR resistance and an output signal that can be modeled as a sensor shunted by a small diode. These unexpected observations, however, do not prevent the use of NSMO sensors on buffered Si as total energy monitors at LCLS.

IV. Summary

We briefly summarize the requirements for the performance of the bolometric total energy monitor (TE) and how the requirements are being met by the above design.

1. Radiation hardness up to 2mJ/pulse: The choice of Si as absorber material makes the TE radiation hard up to 2mJ/pulse. Should thermal fatigue make the sensor brittle upon

prolonged exposure to the LCLS beam, a 20 μm B_4C layer can be added for TE operation at ~2 keV (Section II.A)

2. Dynamic range from 1 μJ to 2 mJ required, to 10 mJ desirable: The TE is sensitive down to an LCLS energy of 1μJ/pulse (Section II.G3 and separate TE electronics ESD 1.5-107). Its linearity has been tested up to 2 mJ/ pulse, and likely extends to higher energies because the TCR of the sensor is constant over several Kelvin. (Section III.B)
3. Range of validity can be calculated. Yes (See Preliminary Design Review)
4. Absolute accuracy of ± 10% at 10 mJ and ± 25% at 10 μJ: The error in absolute accuracy varies between <4 % at 2 mJ/pulse, and <6% at 10 μJ/pulse. It is mostly set by the accuracy of the pulse energy meters used for TE calibration. (Section II.H)
5. Absorbed fraction of the FEL energy calculated: Yes (See Preliminary Design Review)
6. Field of view of 3 mm: Possible for chosen sensor geometry (Section II.D)
7. Remotely movable by at least ± 5 mm: Possible by mounting the TE on a remote-controllable xyz-stage. (Section II.G1)
8. Repeatable to ± 1% at 200 μJ/pulse: Under identical illumination conditions, the repeatability is determined by the preamplifier noise and stability, which is <1% at 200μJ/pulse (Section II.G3 and separate TE electronics ESD 1.5-107)
9. Speed: 10 Hz is required, up to 120 Hz is desirable: TE operation at 180 K is compatible with operating frequencies of 10 Hz and possibly 30 Hz according to figure 2. Operation at 120 Hz is likely not possible unless the fast transient signals can be suppressed to enable operation at ~100 K. (Section II.C)
10. Remotely movable out of FEL radiation zone: Possible by mounting the TE on a remote-controllable xyz-stage (Section G1)
11. Periodic in-situ recalibration: Possible with an optical calibration laser that is integral to the system design (Sections G4 and G5)

V. Continuing Work

While the current TE design meets the requirements for LCLS, there are areas where the TE can be improved.

1) It would be desirable to suppress the fast transients to allow operation at lower temperatures where signal speeds are higher so that the TE can be operated at a repeat frequency of 120 Hz. This may be possible with doped Si substrates where electron-hole life times are shorter.
2) The buffer layer below the NSMO can possibly be modified to suppress the diode like signal shunt path through the substrate and reduce the associated signal loss.
3) The Ti underlayer below the Au contacts to the NSMO could be replaced by Cr to reduce the degradation of the NSMO at the interface to the Au.

We expect other needs for modifications to only become apparent when the TE is exposed to the actual X-ray signals at the LCLS.

References

[1] “XTOD Total Energy Measurement System”, LCLS Physics Requirements Document #1.5-009.

[2] “X-ray interactions: photoabsorption, scattering, transmission, and reflection at E = 50-30000 eV, Z=1-92”, B. L. Henke, E. M. Gullikson, J. C. Davis, *Atom. Data Nucl. Data Tab.* **54**, 181 (1993); see also http://www.cxro.lbl.gov/optical_constants/

[3] “Controlling dose to low Z solids at LCLS”, R. Bionta, Technical Note *LCLS-TN-00-3*.

[4] "Damage threshold of inorganic solids under free-electron-laser irradiation at 32.5 nm wavelength", S. P. Hau-Riege et al., *Appl. Phys. Lett*. **90**, 173128 (2007)

[5] "Thermal stresses in the reflective X-ray optics for the Linac Coherent Light Source", D. D. Ryutov, *Rev. Sci. Instrum*. **74**, 3722 (2003)

[6] "Material characteristics of perovskite manganese oxide thin films for bolometric applications", A. Goyal, M. Rajeswari, R. Shreekala, S. E. Lofland, S. M. Bhagat, T. Boettcher, C. Kwon, R. Ramesh, T. Venkatesan, *Appl. Phys. Lett*. **71**, 2535 (1997)

[7] "Heteroepitaxy of $SrTiO_3$ on vicinal Si(001): Growth and kinetic effects", Y. Liang, Y. Wei, X. M. Hu, Z. Yu, R. Droopad, H. Li, K. Moore, *J. Appl. Phys*. **96**, 3413 (2004)

[8] "Fast Perovskite Manganite Bolometers for Total Energy Measurements of Free Electron X-Ray Lasers", G. J. Yong, Rajeswari M. Kolagani, S. Adhikari, R. M. Mundle, D. W. Cox, A. L. Davidson III, Y. Liang, O. B. Drury, S. P. Hau-Riege, C. Gardner, E. Ables, R. M. Bionta, S. Friedrich, accepted for publication to *Sensor Letters* (2008)

[9] "Design of a bolometer for total energy measurement of the Linac Coherent Light Source pulsed X-ray laser", S. Friedrich, L. Li, L. L. Ott, Rajeswari M. Kolagani, G. J. Yong, Z. A. Ali, O. B. Drury, E. Ables, R. M. Bionta, *Nucl. Inst. Meth.* A **559**, 772 (2006)

[10] "Fabrication of Cryogenic Manganite Bolometers to Measure the Total Energy at the LCLS Free Electron X-ray Laser", O. B. Drury, G. J. Yong, R. M. Kolagani, Y. Liang, C. S. Gardner, E. Ables, K. W. Fong, R. M. Bionta, S. Friedrich, accepted for publication in *IEEE Transactions on Nuclear Science* (2009)

[11] "The charge transport properties of a-Si:H thin films under hydrostatic pressure", W. Hahn, M. Boshta, K. Bärner, R. Braunstein, *Mat. Sci. Eng. B* **130**, 184 (2006)

[12] "Normal and anomalous Dember effect", S. K. Chattopathyaya, V. K. Mathur, *J. Appl. Phys*. **40**, 1930 (1969)

[13] "Pulsed laser-induced transient thermoelectric effects in silicon crystals", M. Sasaki, H. Negishi, M. Inoue, *J. Appl. Phys*. **59**, 796 (1986)